

# A General Calibration Procedure for Measuring RF Voltages and Currents Applied to the EMC Analysis of Automotive High-Voltage Power Networks

Christian Zietz, *Student Member, IEEE*, Gunnar Armbrrecht, *Member, IEEE*, Thomas Schmid, *Member, IEEE*, Michael Wollitzer, *Member, IEEE*, and Bernd Geck, *Member, IEEE*

**Abstract**—This paper presents a general calibration procedure for probing RF voltages and currents in the time domain with conventional oscilloscopes using a directional coupler. It eliminates the need for a separate power calibration and takes advantage of the large dynamic range of a vector network analyzer during the calibration step. As a first application of this procedure, the electromagnetic disturbances on high-voltage (HV) lines in vehicles with hybrid or electric drive are precisely determined by applying an HV automotive-grade directional line coupler. In conjunction with the calibration algorithm, this coupler permits measuring the EMI relevant noise voltages and currents during real operation conditions of the vehicle without the need to modify the HV network by inserting LISNs or other artificial networks. The presented HV coupler offers a superior RF performance between its HV ports yielding an insertion loss of max. 0.8 dB and a return loss of min. 15 dB with respect to a typical low characteristic impedance of HV lines of  $11\ \Omega$  over a frequency range from 150 kHz to 1 GHz. Thus, the coupler itself causes minimal influence on the original waveforms within the HV network and facilitates measurements very close to the noise sources, e.g., the power inverter, at a distinct calibration plane. Furthermore, it is shown how the accurate knowledge of these voltages and currents can be utilized to predict radiated emissions or to derive load impedances. Herein, the measurements are performed in a CISPR 25 related setup over a frequency range from 150 kHz to 500 MHz, achieving a good agreement to conventional measurement methods.

**Index Terms**—Calibration, CISPR 25, current measurement, electric vehicles (EVs), electromagnetic disturbances, high-voltage (HV) automotive power networks, hybrid vehicles, ISO 7637-4, voltage measurement.

## I. INTRODUCTION

WITH the advent of hybrid electric vehicles (HEV) and full electric vehicles (EV) spurred worldwide by legislative activities, electromagnetic compatibility of the high-voltage (HV) power network is an increased challenge [1]. In Fig. 1, a typical topology of an HV network in an electric vehicle is shown including major components like, e.g., the battery, the

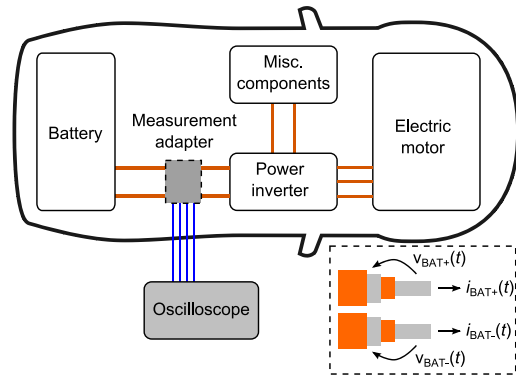


Fig. 1. Typical topology of an HV network in an electric vehicle including a setup to independently measure voltages  $v(t)$  and currents  $i(t)$  on the coaxially shielded HV lines.

power inverter and the motor. High-power electronics cause fast switching transients and the HV network becomes the origin of electromagnetic interference. Therefore, shielding all components is mandatory to ensure that the entire HV system is able to meet the stringent limits of automotive EMC standards. Each HV line often consists of a coaxially shielded cable that has a large inner conductor due to the current carrying requirements, and thus, exhibits a low characteristic RF impedance of approximately  $9\text{--}12\ \Omega$  [2].

Recent EMC research activities in this field include the impedance characterization of HV components [2], [3], optimization of the design of EMC filters [4], and the creation of more accurate simulation models of entire HV networks [5]. In order to support the activities mentioned earlier, the electromagnetic disturbances on the HV lines need to be known during regular operation of all components, since every component can be the source of unwanted disturbances. This measurement task is characterized by the fundamental need to determine magnitude and phase of voltages and currents over a wide spectral range from 150 kHz to 1 GHz (related to CISPR 25 [6]) at a distinct reference plane, i.e., at a distinct location along the line. It is advantageous to measure these quantities in the time domain since in this case all phase relations are inherently preserved. Thus, even arbitrary waveforms such as nonperiodic signals like single pulse events can be detected. However, dc components of voltage and current need not to be measured, when solely focusing on electromagnetic disturbances. Furthermore, for safety reasons, galvanic isolation between HV lines and measurement devices is essential.

Manuscript received November 7, 2014; revised April 19, 2015; accepted May 27, 2015. Date of publication June 23, 2015; date of current version October 12, 2015.

C. Zietz and B. Geck are with the Institute of Radiofrequency and Microwave Engineering, Leibniz Universität Hannover, 30167 Hannover, Germany (e-mail: zietz@hft.uni-hannover.de; geck@hft.uni-hannover.de).

G. Armbrrecht, T. Schmid, and M. Wollitzer are with the Rosenberger Hochfrequenztechnik GmbH & Co. KG, 83413 Fridolfing, Germany (e-mail: Gunnar.Armbrrecht@rosenberger.de; Thomas.Schmid@rosenberger.de; Michael.Wollitzer@rosenberger.de).

Color versions of one or more of the figures in this paper are available online at <http://ieeexplore.ieee.org>.

Digital Object Identifier 10.1109/TEM.2015.2442522

Fig. 1 shows an exemplary setup to record the voltages and currents on the battery lines of an electric vehicle. For instance, the HV cables of the battery line are split up and a measurement adapter is inserted to provide a connection to an oscilloscope. Conventional solutions utilize voltage dividers [7], Rogowski coils [8], shunt resistors, Hall sensors, current probes, or artificial networks [9]. However, these methods are often unable to correctly acquire the RF portion of the signals or the adapter itself modifies the network to such an extent that the EMI relevant signals are distorted [10]. Furthermore, many of them do not offer a user-definable reference or calibration plane. Such a single reference plane for voltage and current is required for an accurate calculation of the frequency-dependent impedances of components in the HV network during its operation. Their knowledge is vital for tasks such as the optimization of EMC filters or the design of line impedance stabilization networks suitable for HV harnesses [2].

Therefore, this study presents a broadband RF measurement system for voltages and currents, based on a novel calibration procedure that applies low insertion loss directional couplers with matching RF line impedance. It should be noted that the presented procedure is not restricted to EMC applications. There is no inherent limitation of the frequency range in the algorithms described later. Thus, the procedure is also suited for RF and microwave measurements, such as device characterization. This paper is structured as follows: Section II presents the mathematical derivation of the calibration of the measurement system performed in the frequency domain using a vector network analyzer (VNA). In Section III, the time-domain measurement based on the previous calibration is shown and the influence of possible errors is illustrated in Section IV. As this paper focuses on the measurement of EMI relevant noise phenomena in HV networks, in Section V, a directional line coupler is introduced, which is specifically developed for the application in automotive HV networks. In Section VI, the implementation of the measurement system is verified by measuring voltages and currents using the presented HV directional line coupler. Advantageous applications of the presented measurement framework—predicting radiated emission measurements and calculating load impedance—are illustrated in Section VII. Finally, the work is summarized in Section VIII.

## II. THEORY OF CALIBRATION

The calibration of a measurement setup is a well-known technique for removing systematic errors from the measurement like, e.g., the influence of the measurement accessories. Additionally, defining a specific calibration plane, to which voltage and current are referenced, becomes unavoidable at frequencies where the lines become electrically long. While at 150 kHz even HV lines with a length of several meters can be considered electrically short, at 1 GHz, the same line lengths easily exceed the wavelength. Therefore, the transformation of voltages and currents along the line according to the transmission line theory [11] has to be taken into account, thus requiring one single reference plane for both voltage and current.

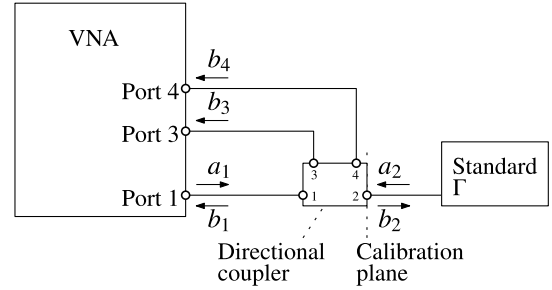


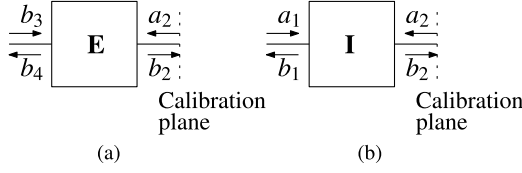
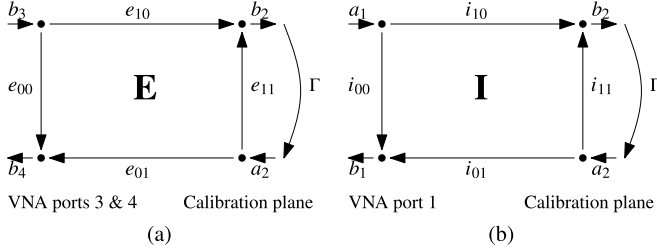
Fig. 2. Setup for calibration of the measurement system.

In RF and microwave engineering, it is common practice to characterize linear devices in the frequency domain by measuring small-signal reflections coefficients and scattering parameters in a defined calibration plane [12]. For this purpose, multiple calibration methods for VNAs have been developed [13]. However, the measurement method presented in this study is required to measure large signal quantities in order to be prepared even for the characterization of nonlinear devices. Considerably more effort is needed for the calibration to conduct frequency-domain measurements of such nonlinear devices [14]. For example, to characterize devices by their X-parameters, further calibration steps involving a power meter and a phase reference are needed [15]. The calibration of a setup to measure voltages and currents in the time domain—as proposed in this paper—does not require a phase reference generator. However, conventional methods utilized for such setups still utilize a separate calibration step to obtain a power reference [16]–[20].

The measurement procedure presented herein skips this additional power calibration step, by utilizing three test ports of a VNA, as it will be shown in Section II-A. While the measurement itself is performed in the time domain, the calibration is carried out in the frequency domain, because the VNA's higher dynamic range yields more accurate calibration results compared to an oscilloscope.

### A. Calibration Algorithm

The setup for calibrating the measurement system consisting of a directional coupler and cables by means of a VNA is shown in Fig. 2. In order to measure scattering parameters  $\tilde{S}_{x1} = b_x/a_1$ , the VNA generates an incident wave  $a_1$  and measures the reflected wave quantities  $b_x$ . A previous calibration of the VNA itself ensures that no other incident waves exist, i.e., it is asserted that  $a_3 = a_4 = 0$ . The directional coupler and any necessary cables can be regarded as a four-port. Its ports 1, 3, and 4 are connected to the respective ports of the VNA, while the port 2 forms the calibration plane, to which the calibration standards are connected. This four-port can be divided into two two-ports **E** and **I**, which are shown in Fig. 3. Similar to the theory of calibration of VNAs [12] a two-port **E** with the scattering parameters  $e_{xy}$  (also referred to as error terms) can be defined by means of the four-port / two-port reduction [21]. This two-port is located between the ports 3 and 4 of the VNA and the calibration plane. It does not depend on conditions at port 1


 Fig. 3. Resulting error two-ports (a) Two-port **E** (b) Two-port **I**.

 Fig. 4. Signal flow graphs. (a) Two-port **E**. (b) Two-port **I**.

(VNA source/generator) of the original four-port. Furthermore, while  $b_3$  is a reflected wave in the original four-port, it is as an incident wave after the four-port / two-port reduction.

The two-port **I** with the error terms  $i_{xy}$  is located between port 1 of the VNA and the calibration plane. For the derivation of **I**, the ports 3 and 4 of the original four-port are considered to be terminated by the corresponding input impedance of the VNA. The signal flow graphs relating incident and reflected wave quantities ( $a_n$ ,  $b_n$ ) to the error terms  $e_{xy}$  and  $i_{xy}$  are depicted in Fig. 4.

The calibration procedure determines all four error terms  $e_{xy}$ , as these describe the relation between the wave quantities  $a_2$  and  $b_2$  in the calibration plane and the quantities  $b_3$  and  $b_4$  at the coupled ports. During a subsequent measurement only  $b_3$  and  $b_4$  are measured, as shown in Section III. Based on these quantities and the error terms  $e_{xy}$ , the wave quantities and the voltage and current in the calibration plane are calculated.

The wave quantities  $a_2$  and  $b_2$ , and hence, the reflection coefficient  $\Gamma = a_2/b_2$  refer to a system impedance  $Z_1$ , which is chosen during the calibration.  $Z_1$  does not need to be the physical line impedance in the calibration plane, which may even be unknown. It can be chosen during calibration and needs to be retained during measurement, as will be shown in (12).

From the signal flow graph in Fig. 4(a), the reflection coefficient  $\Gamma$  in the calibration plane can be expressed in terms of measurable quotients of wave quantities [13].

$$\Gamma = \frac{b_4/b_3 - e_{00}}{e_{10}e_{01} + e_{11}(b_4/b_3 - e_{00})}. \quad (1)$$

where  $b_4/b_3$  is equal to  $\tilde{S}_{41}/\tilde{S}_{31}$ . An equation similar to (1) can be found from Fig. 4(b) relating  $\Gamma$  to  $b_1/a_1 = \tilde{S}_{11}$  utilizing the error terms  $i_{xy}$ . If three calibration standards with known different reflection coefficients  $\Gamma$  are affixed to the calibration plane, two systems of three equations can be established that can be solved for  $e_{00}$ ,  $e_{10}e_{01}$ , and  $e_{11}$  and  $i_{00}$ ,  $i_{10}i_{01}$ , and  $i_{11}$ , respectively. If the three standards are an Open ( $\Gamma_O \approx 1$ ), a

Short ( $\Gamma_S \approx -1$ ), and a nonreflecting Match ( $\Gamma_M = 0$ ), this results in the well-known OSM calibration procedure [12], as it is exemplarily shown for **E**.

$$e_{00} = \frac{\tilde{S}_{41,M}}{\tilde{S}_{31,M}} \quad (2)$$

$$e_{10}e_{01} = \frac{(\Gamma_O - \Gamma_S)(\frac{\tilde{S}_{41,O}}{\tilde{S}_{31,O}} - \frac{\tilde{S}_{41,M}}{\tilde{S}_{31,M}})(\frac{\tilde{S}_{41,S}}{\tilde{S}_{31,S}} - \frac{\tilde{S}_{41,M}}{\tilde{S}_{31,M}})}{\Gamma_O \Gamma_S (\frac{\tilde{S}_{41,O}}{\tilde{S}_{31,O}} - \frac{\tilde{S}_{41,S}}{\tilde{S}_{31,S}})} \quad (3)$$

$$e_{11} = \frac{\Gamma_S (\frac{\tilde{S}_{41,O}}{\tilde{S}_{31,O}} - \frac{\tilde{S}_{41,M}}{\tilde{S}_{31,M}}) - \Gamma_O (\frac{\tilde{S}_{41,S}}{\tilde{S}_{31,S}} - \frac{\tilde{S}_{41,M}}{\tilde{S}_{31,M}})}{\Gamma_O \Gamma_S (\frac{\tilde{S}_{41,O}}{\tilde{S}_{31,O}} - \frac{\tilde{S}_{41,S}}{\tilde{S}_{31,S}})}. \quad (4)$$

$i_{xy}$  are derived by replacing  $\tilde{S}_{41}/\tilde{S}_{31}$  by  $\tilde{S}_{11}$  in (2)–(4). While the error terms ascertained during the aforementioned calibration suffice to calculate reflection factors of arbitrary devices [13] using (1), they are inadequate to determine the absolute wave quantities  $a_2$  and  $b_2$ . This requires the separation of the product  $e_{10}e_{01}$  into individual error terms. This information cannot be obtained by an OSM calibration, or even by simply adding further one-port calibration standards, as (1) cannot be solved for  $e_{10}$  and  $e_{01}$  individually. Hence, an additional calibration step is proposed by [16]–[20], during which the calibration plane is connected to a port of a device (oscilloscope or power meter) by means of a Through standard to obtain a power reference measurement, ultimately yielding  $e_{10}$ . The scattering parameters of this Through standard need to be known, which can be challenging, especially if the calibration plane is not a 50-Ω coaxial interface.

In contrast, the calibration procedure presented in this study does neither require a Through standard nor further steps other than the measurement of the three standards mentioned previously. This can be achieved by exploiting the secondary error two-port **I**. It is worth noting that the main error two-port **E** is generally nonreciprocal, i.e.,  $e_{10} \neq e_{01}$ . However, the two-port **I** describes the relation between port 1 of the VNA and the calibration plane and can thus be assumed to be reciprocal, when a passive directional coupler is used.

$$i_{10} = i_{01} = \pm \sqrt{i_{10} \cdot i_{01}}. \quad (5)$$

The correct sign in (5) can be chosen if the approximate electrical length of the setup between port 1 of the VNA and the calibration is known.

From Fig. 4, the following equations can be derived for the wave quantity  $b_2$ :

$$b_2 = \frac{i_{10}a_1}{1 - i_{11}\Gamma} \quad (6)$$

$$b_2 = \frac{e_{10}b_3}{1 - e_{11}\Gamma}. \quad (7)$$

Since both equations describe the same wave quantity, the error term  $e_{10}$  can be expressed as

$$e_{10} = i_{10} \cdot \frac{a_1}{b_3} \cdot \frac{1 - e_{11}\Gamma}{1 - i_{11}\Gamma} \quad (8)$$

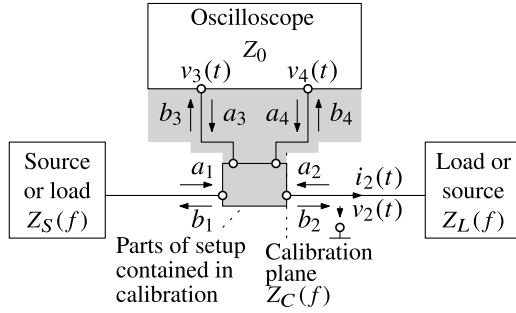


Fig. 5. Setup for measurement of voltage and current; parts that must not be changed between calibration and measurement are marked in gray.

where  $a_1/b_3 = \tilde{S}_{31}^{-1}$ . Thus,  $e_{10}$  and  $e_{01}$  can be calculated separately from (3) as required. Inserting (1) in (7) and using

$$a_2 = \frac{b_4 - e_{00}b_3}{e_{01}} \quad (9)$$

the wave quantities in the calibration plane can be determined utilizing solely the error two-port **E** and the measured quantities  $b_3$  and  $b_4$ .

### B. Summary of Calibration Workflow

The following steps need to be executed to calibrate the measurement setup:

- 1) calibrate the four-port VNA itself at its ports 1, 3, and 4 using a conventional calibration procedure;
- 2) connect the directional coupler to the VNA as shown in Fig. 2;
- 3) successively connect the calibration standards (e.g., Open, Short, and Match) to the calibration plane of the directional coupler, measuring  $\tilde{S}_{11,x}$ ,  $\tilde{S}_{31,x}$ , and  $\tilde{S}_{41,x}$ ;
- 4) evaluate (2)–(4) to get  $e_{00}$ ,  $e_{10}e_{01}$ ,  $e_{11}$ ,  $i_{00}$ ,  $i_{10}i_{01}$ , and  $i_{11}$ .
- 5) compute  $i_{10}$  by (5), and thus, the complete error two-port **I**, and finally, calculate  $e_{10}$  and  $e_{01}$  using (8), yielding a complete error two-port **E**.

## III. THEORY OF MEASUREMENT

As already mentioned in Section I, a time-domain measurement (e.g., with an oscilloscope or with any other sampling device) is applied since it inherently captures broadband signals including single-shot events preserving all magnitude and phase information. Fig. 5 shows the proposed measurement setup. The oscilloscope captures the voltages  $v_3(t)$  and  $v_4(t)$  at the coupled ports of the coupler. The calibration procedure shown in Section II allows to calculate voltage  $v_2(t)$  and current  $i_2(t)$  in the defined calibration plane from this data.

The application of the error terms  $e_{xy}$  is illustrated in the following. These error terms only describe the part of the setup highlighted in gray in Fig. 5, i.e., the coupler up to the calibration plane and the cables connecting the coupler to the oscilloscope. Hence, changes of the remaining elements such as the

impedance of the source ( $Z_S$ ) or of the load ( $Z_L$ ) theoretically have no influence on the correctness of the measurement.

To apply the error terms  $e_{xy}$  as frequency-domain quantities, the raw voltages  $v_3(t)$  and  $v_4(t)$  are transformed into their frequency-domain representations  $V_3(f)$  and  $V_4(f)$  by means of a fast Fourier transform (FFT).<sup>1</sup> The voltages are sampled by the oscilloscope in discrete time intervals  $\Delta t$ . They are assumed to be bandwidth limited to  $f_{\max} = 1/(2\Delta t)$  to fulfill the sampling theorem. Thus, the voltages are to be designated as

$$v_3[k] = v_3(k \cdot \Delta t) \quad (10a)$$

$$v_4[k] = v_4(k \cdot \Delta t). \quad (10b)$$

If a total number of  $N$  samples is considered, the following frequency-domain representation of the wave quantities  $b_3$  and  $b_4$  is given by the Fourier transform [22].

$$b_3[n] = \sqrt{Z_0}^{-1} \sum_{k=0}^{N-1} v_3[k] e^{-jkn \cdot 2\pi/N} \quad (11a)$$

$$b_4[n] = \sqrt{Z_0}^{-1} \sum_{k=0}^{N-1} v_4[k] e^{-jkn \cdot 2\pi/N} \quad (11b)$$

$$\text{for } n = 0, 1, \dots, N-1$$

where  $Z_0$  is the input impedance of the oscilloscope (usually 50  $\Omega$ ), assuming a negligible mismatch at the input ports of the oscilloscope.

Utilizing these wave quantities as well as (1), (7), and (9)—resampling the error terms  $e_{xy}$  in frequency domain as required—yields the absolute wave quantities  $a_2$  and  $b_2$  in the calibration plane, from which voltage and current can be determined independently from each other:

$$V_2[n] = \sqrt{Z_1} \cdot (a_2[n] + b_2[n]) \quad (12a)$$

$$I_2[n] = \sqrt{1/Z_1} \cdot (a_2[n] - b_2[n]) \quad (12b)$$

where  $Z_1$  is the system impedance chosen as reference for the reflection coefficients as stated in Section II-A. From  $V_2[n]$  and  $I_2[n]$ , the time-domain representations  $v_2[k]$  and  $i_2[k]$  can be found by means of an inverse fast Fourier transform (IFFT).

A simplified flow graph of the whole measurement procedure derived herein is presented in Fig. 6. The voltage and current in the calibration plane cause signals to be coupled out—shown here only for measurement port 3 of the coupler. This signals can optionally be windowed prior to further processing, for example, by using a Hann window function. The signals are transformed into the frequency domain (compare (11)). Note that only the magnitude is shown in Fig. 6, however, the phase also needs to be taken into account and must not be discarded. After the application of (1), (7), and (9), the frequency and time-domain representations of the voltage in the calibration plane—weighted with the chosen window function—are known. A very good agreement between  $v_2(t)$  in the lower right corner and the reference voltage in the upper left corner can be observed within time interval of the respective window function.

<sup>1</sup> If huge amounts of data need to be processed, a short-term Fourier transform (STFT, [22]) may also be used to process multiple blocks of data separately.



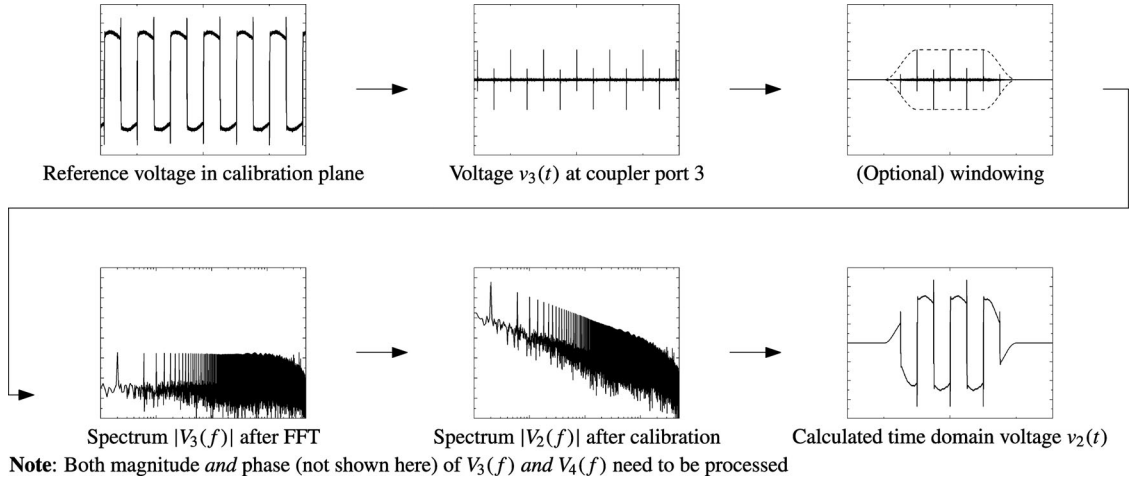


Fig. 6. Simplified scheme of the application of the calibration terms to the measurement data.

#### IV. INFLUENCES OF ERRORS

In this section, two sources of measurement errors particularly relevant for practical measurements are investigated: additional attenuation or delay caused, for example, by different cables connecting the directional coupler to the oscilloscope as well as oscilloscope noise.

##### A. Additional Cables or Attenuators

As shown in Fig. 5, the cables connecting the directional coupler to the oscilloscope are included in the error terms, and therefore, they should not be changed between calibration and measurement. However, depending on the actual measurement setup, sometimes it may be unavoidable to add mechanical adapters or even attenuators or amplifiers not present during the calibration to the coupled ports of the coupler. Hence, the effects of such elements on the measurement results need to be analyzed.

Assuming negligible mismatch between the components, the measured wave quantities  $\tilde{b}_3$  and  $\tilde{b}_4$  are defined as follows:

$$\tilde{b}_3 = k_1 \cdot b_3 \quad (13a)$$

$$\tilde{b}_4 = k_2 \cdot b_4 \quad (13b)$$

where  $k_{1,2}$  account for any additional attenuation, amplification or delay. If the same attenuation/amplification is considered at both ports ( $k_1 = k_2 = k \in \mathcal{R}$ ), as it can be often assumed in practice, (1) is not affected and the erroneously calculated quantities in the calibration plane can be stated with (7) and (9) as  $\tilde{a}_2 = ka_2$  and  $\tilde{b}_2 = kb_2$ . Hence, the calculated voltage  $\tilde{V}_2[l]$  and current  $\tilde{I}_2[l]$  calculated by (12) be corrected for known attenuation/amplification by simply dividing by  $k$ .

If the same delay  $\tau$  is present at both measurement ports, e.g., caused by additional adapters, this can be considered by a frequency-dependent phase shift  $k = k_1 = k_2 = e^{-j\tau 2\pi f}$  in  $\tilde{a}_2$  and  $\tilde{b}_2$  as well as in the frequency-domain representations of voltage and current. The time-domain waveforms  $\tilde{v}_2(t)$  and  $\tilde{i}_2(t)$ , obtained by IFFT, can thus be corrected by simply shifting them by  $-\tau$  in time. These simple corrections cannot be applied

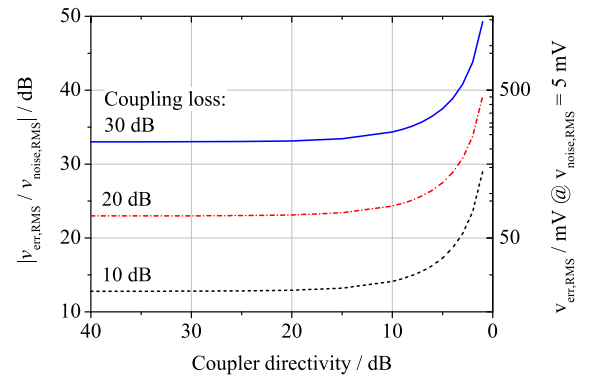


Fig. 7. Influence of coupler parameters on the measurement error.

if unequal attenuation or delay is present. Thus, this case should be avoided.

##### B. Oscilloscope Noise

The noise of the oscilloscope itself, including the error introduced due to quantization [23], can be viewed as additive noise. To investigate this effect, white Gaussian noise having the RMS value  $v_{\text{noise,RMS}}$  is added to the raw voltages  $v_3(t)$  and  $v_4(t)$  and its effect on the voltage  $v_2(t)$  is accounted for by calculating the error voltage  $v_{\text{err}}(t)$  superimposed on the undistorted voltage in the calibration plane. As the system is linear and time invariant,  $v_{\text{err}}$  does not depend on the undistorted signal and it can be normalized with respect to  $v_{\text{noise}}$ .

1) *Frequency-Independent Coupler*: To gain fundamental insights into the influences of oscilloscope noise on the measurement error, simulations using an analytically defined coupler (with port numbers as defined in Fig. 2) are performed. This coupler is based on the four-port scattering parameters  $S_{xy}$  of the ideal directional coupler [11], with added finite isolation ( $S_{41} \neq 0$ ), while still maintaining passivity. Thus, coupling loss  $1/|S_{31}|$  and directivity  $|S_{31}|/|S_{41}|$  can be chosen arbitrarily and without frequency dependence. Fig. 7 shows the error voltage

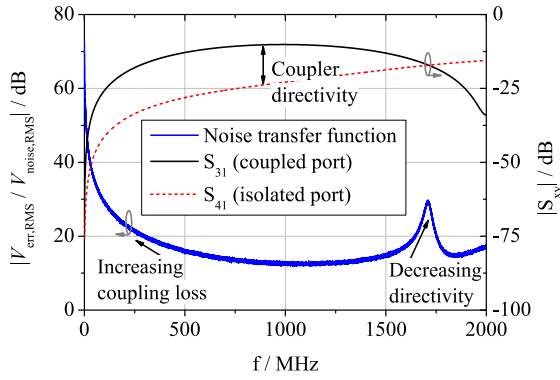


Fig. 8. Frequency-dependent noise transfer function for an exemplary directional coupler.

in the calibration plane ( $v_{\text{err,RMS}}$ ) normalized with respect to the assumed noise level at the ports of the oscilloscope ( $v_{\text{noise,RMS}}$ ). Given a constant undistorted signal voltage an increasing coupling loss causes a decreasing signal-to-noise ratio and a larger error. Thus, it can be seen that the error in decibel is related linearly to the coupling loss in decibel. However, it can also be noted that the error strongly depends on the coupler directivity, i.e., the ability of the coupler to differentiate between incident and reflected waves. While the theory presented in Sections II and III imposes no restrictions on the directivity of the coupler, under the additional assumption of oscilloscope noise, the performance of the measurement system degrades when low directivity couplers are utilized. For example, the error increases by 3 dB at a directivity of only 6.6 dB compared to a coupler with ideally isolated ports. In Fig. 7, additional values for the error voltage are given assuming an RMS value of the noise of 5 mV at the oscilloscope's ports.

2) *Frequency-Dependent Coupler*: However, common directional couplers rarely exhibit a frequency-independent behavior. In order to account for this fact, a simulation is performed using a model of a microstrip line directional coupler [11], whose scattering parameters  $S_{31}$  and  $S_{41}$  are shown in Fig. 8. As in Section IV-B1,  $|S_{31}|^{-1}$  is the coupling loss,  $|S_{41}|^{-1}$  the isolation, and hence,  $|S_{31}|/|S_{41}|$  is the directivity of the coupler. The minimum coupling loss is achieved at 1 GHz and the directivity decreases above 1 GHz and becomes 0 dB at approx. 1.7 GHz.

Fig. 8 depicts the noise transfer function, i.e., the spectral density of the error voltage in the calibration plane normalized to the spectral density of the noise voltage assumed at the oscilloscope's ports. From 1 GHz down to dc the increasing coupling loss dominates the error, whereas above 1 GHz, it is mostly influenced by the decreasing directivity. Utilizing Figs. 7 and 8, a directional coupler providing a sufficient signal-to-noise ratio can be designed if the RMS value of the noise of the oscilloscope is known.

## V. HV DIRECTIONAL LINE COUPLER

In order to apply the presented measurement system to an HV power network of an electric vehicle, a setup as depicted

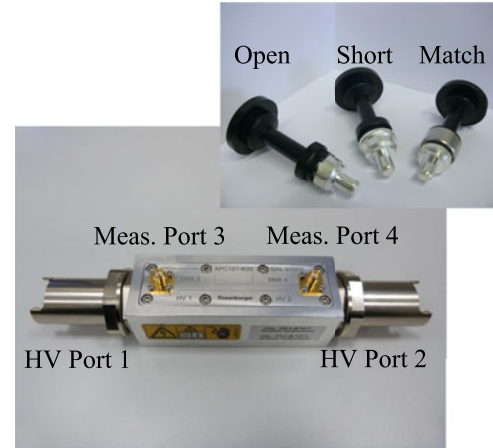


Fig. 9. HV directional line coupler and OSM calibration standards.

in Fig. 1 is proposed. Instead of a conventional measurement adapter, a directional line coupler is inserted into each of the coaxially shielded HV lines of interest, like, e.g., the battery lines, and connected to an oscilloscope. This, then, allows the measurement of the single-ended voltage (i.e., between inner conductor and ground) as well as the current on the inner conductor of the HV lines. A directional line coupler is chosen because it can be optimized to match the line impedance and to exhibit a low insertion loss [24], [25]. Therefore, inserting an optimized automotive-grade directional line coupler into the HV line should minimize the influence on the network under test.

Fig. 9 shows the automotive-grade HV directional coaxial line coupler [26] developed in conjunction with the presented measurement framework, suitable for broadband measurements from 150 kHz to 1 GHz, as postulated in Section I. The coupler has been designed with particular emphasis on its RF performance, as the measurement system must have only negligible influence on the HV network. Hence, a coupler is required that retains the shielding of the HV network and is specifically designed to be matched to the line impedance of the HV network of approximately 11  $\Omega$  [2].

The scattering parameters  $S_{31}$  and  $S_{41}$  of the HV line coupler are shown in Fig. 10. It can be seen that the coupler maintains a directivity of at least 10 dB up to 1 GHz, hence, reducing the detrimental effects of oscilloscope noise as shown in Section IV-B1. Since the line coupler is shorter than a quarter wavelength, it exhibits a frequency-dependent coupling loss that compensates the expected spectral distribution of the noise voltage [27], therefore, ensuring an approximately constant spectral voltage density of  $v_3(t)$  and  $v_4(t)$  at the oscilloscope ports,<sup>2</sup> advantageously compressing the dynamic range of the HV signal at the measurement ports.

Further properties of the HV directional coupler include:

- 1) utilizable frequency range: 150 kHz–1 GHz;
- 2) insertion loss (HV ports): max. 0.8 dB;
- 3) return loss (HV ports): min. 15 dB;

<sup>2</sup>This can also be seen in the spectrum after the FFT in Fig. 6.

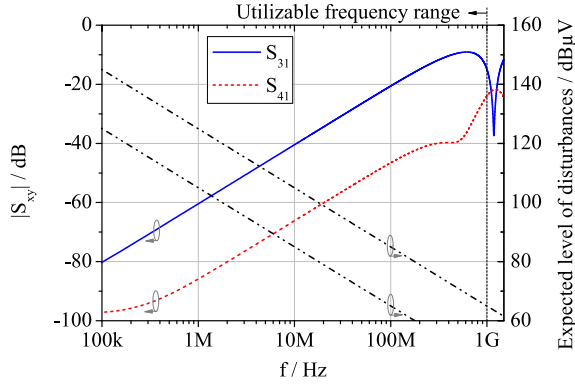


Fig. 10. Scattering parameters  $S_{31}$  and  $S_{41}$  of an HV coupler and upper and lower bounds for the expected level of disturbances within the HV power network.

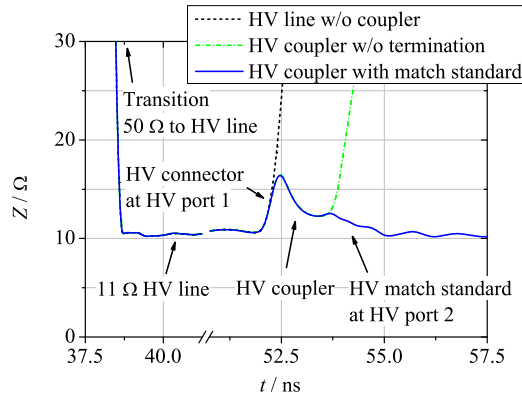


Fig. 11. TDR of the impedance  $Z$  of an HV coupler and match standard (at 250 ps rise time  $\hat{=}$  1.4 GHz bandwidth).

- 4) HV test voltage: 2700 V dc;
- 5) temperature range:  $-40$ – $125$  °C;
- 6) HV current carrying capacity: 230 A at 85 °C ambient temperature.

The HV interface of the coupler utilizes connectors that—while primarily designed for a high current carrying capability—also offer an acceptable RF performance. Suitable nonmetrology OSM standards have also been manufactured. Although these standards are not traceable due to their HV interface, care has been taken to ensure definite reflection coefficients over the entire frequency range. Time-domain reflectometry (TDR) plots with a rise time of 250 ps (corresponding to 1.4 -GHz bandwidth) showing the characteristic impedance  $Z$  of the HV coupler and associated components are depicted in Fig. 11. The HV line without coupler is also shown for temporal reference. It can be seen that the biggest reflection ( $16.4\Omega$ ) originates from the HV connector, while the line coupler itself as well as the corresponding match standard are very well adapted to the impedance of the HV line.

Fig. 12 emphasizes the importance of an optimized measurement adapter—like the presented HV coupler. A situation as depicted in Fig. 1 is considered in a simulation: Differential battery lines, having a length of 7 m and a characteristic impedance

of  $11\Omega$  are excited by a trapezoidal signal with a fundamental frequency of 10 kHz. Its spectrum is shown in Fig. 12. When a conventional measurement adapter is inserted into the HV battery lines, a mismatch in the line impedance as well spurious coupling between both lines occurs. This excites additional resonances starting above 10 MHz in this example, which can also appear in the FM radio band. Thus, the user may be misled by erroneous levels of electromagnetic disturbances that, however, do not represent the situation within the HV power network itself but that are only caused by the measurement adapter. In contrast, the HV directional coupler is designed not to modify the properties of the HV line. With two HV couplers inserted into the network, the user is able to measure the undistorted signal as it is present on the HV line during normal operation, as can be seen from Fig. 12. This is a considerable advantage compared to conventional measurement adapters that significantly change the measured signal [10].

## VI. VERIFICATION MEASUREMENTS

In order to verify the measurement procedure derived in Sections II and III, calibration and measurements utilizing the HV directional line coupler are performed, as depicted in Fig. 13. First, the calibration plane of the coupler is connected to a third input channel of the oscilloscope via a previously characterized attenuator, resulting in the ability to measure a reference voltage. Thus, the load seen in the calibration plane is the input impedance of the attenuator. A trapezoidal signal with a fundamental frequency of 200 kHz is generated by an RF source. The signal is amplified and fed into the HV port of the coupler. Fig. 14 shows an excellent agreement between the directly measured reference voltage and the voltage  $v_2(t)$  calculated by the algorithms as described herein. Notably, the high-frequency components present in the switching transients [see Fig. 14(b)] are measured correctly, as well. Furthermore, the current  $i_2(t)$ , which is independently derived, shows a good agreement with the values expected due to the 50- $\Omega$  input impedance of the attenuator.

In order to highlight the broadband measurement capability of the presented system, the spectrum  $|V_2(f)|$  obtained by FFT from  $v_2(t)$  is compared to a reference measurement using an EMI test receiver connected to the calibration plane via the attenuator. Fig. 15 shows the envelope curve of both spectra, and thereby, confirms that the proposed system correctly measures even high-frequency EMI. The deviation to the test receiver is less than  $\pm 3$  dB up to 300 MHz. The increasing absolute errors at higher frequencies are primarily caused by the limited bandwidth of the test signal, arising from the generator's rise time  $t_{\text{rise}} = 1$  ns.

## VII. APPLICATIONS IN A CISPR 25 RELATED SETUP

Measurements with the HV coupler inside the differential battery lines of a car, as depicted in Fig. 1, are shown in [27] and [28] highlighting among others the ability to combine two single-ended measurements to gain insight about common-mode currents on the shield of the HV lines. In this paper, two further applications of the measurements enabled by the HV coupler

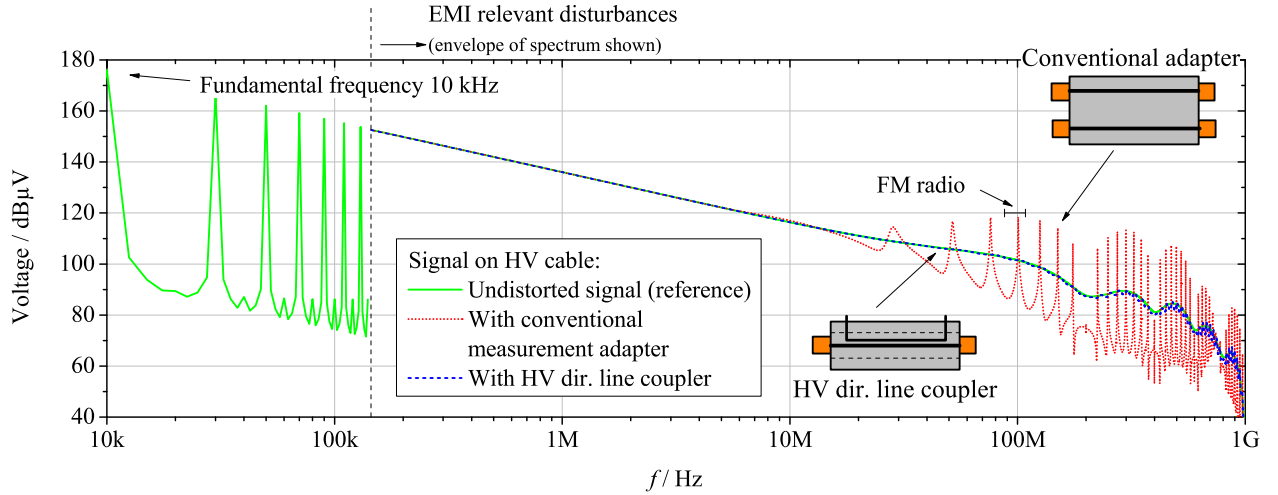


Fig. 12. Simulated influence of the measurement adapter on the spectrum on the HV battery line (length = 7 m). Only envelope curve of the spectrum shown above 150 kHz.

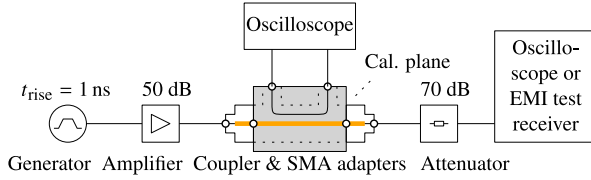


Fig. 13. Verification measurements with HV coupler and oscilloscope or EMI test receiver.

are introduced and verified in a CISPR 25 [6] related setup: the prediction of radiated emissions and the determination of load impedances under operating conditions.

#### A. Predicting Radiated Emissions

In compliance to CISPR 25 [6], emissions of components or wire harnesses, such as the HV lines, are commonly measured using an EMI test receiver connected to an antenna placed inside an absorber-lined shielded enclosure (ALSE) together with the device under test as depicted exemplarily in Fig. 16. If a multitude of operating conditions have to be considered, numerous time-consuming measurements need to be done inside the ALSE. A method for more efficient simulation of such a setup is presented in [29]. However, for an accurate simulation, the source of radiated emissions needs to be known. Hence, in this section, it is investigated whether the knowledge of voltages and currents on an HV line gained by the presented measurement procedure can be utilized to predict said emission measurements.

For this purpose, a lab setup related to those described in CISPR 25 and depicted in Fig. 17 is used to obtain a comparison to a traditional emission measurement. A section of an HV line with a previously calibrated HV directional coupler is fed by the same generator and amplifier as in Section VI and it is terminated by a mismatched 50-Ω load. In the reference measurement, an antenna (rod or monopole antenna for  $f = 150 \text{ kHz} - 30 \text{ MHz}$ , BiLog antenna for  $f = 30 - 500 \text{ MHz}$ ) is connected to an EMI

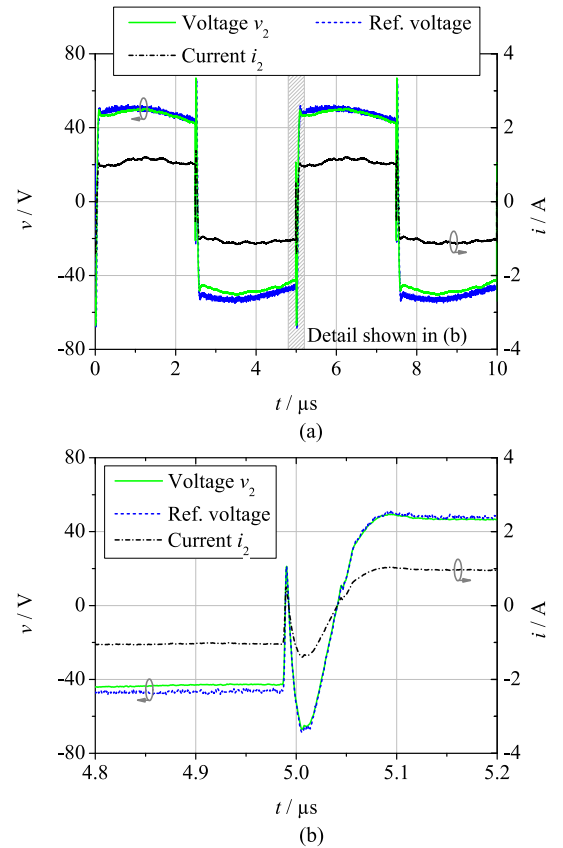


Fig. 14. Voltage  $v_2(t)$  and current  $i_2(t)$  in the calibration plane (calculated independently of each other) versus directly measured reference voltage. (a) Trapezoidal test signal. (b) Detailed view of fast switching transients.

receiver. In a second measurement setup—shown in the inset in Fig. 16—the outputs voltages at the coupler are measured by an oscilloscope and utilized to calculate the wave quantities  $a_2$  and  $b_2$  as well as voltage  $v_2$  and current  $i_2$  in the calibration plane as described by (7), (9), and (12). This setup allows to compare the emission measurement with the EMI receiver with



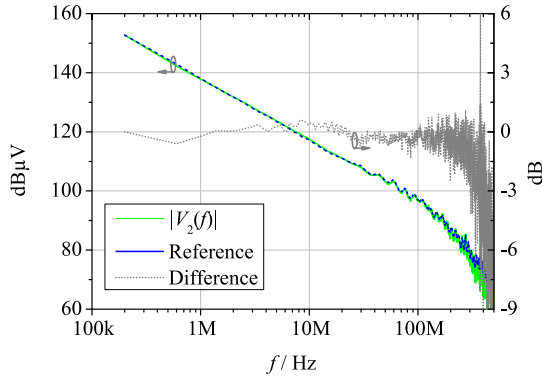


Fig. 15. Envelope of spectrum of the verification signal versus EMI test receiver as reference.

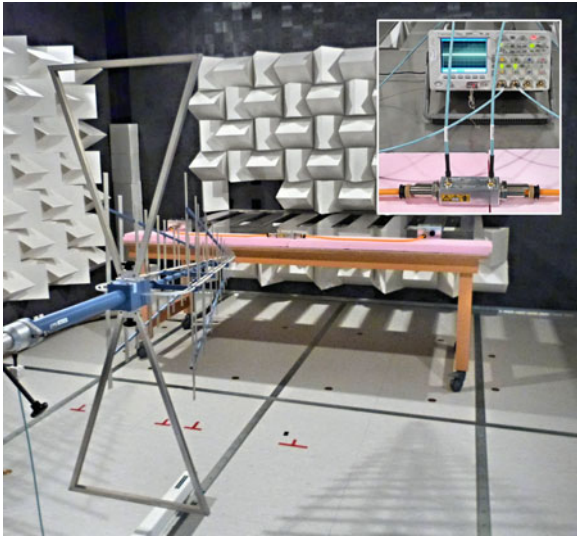


Fig. 16. Reference measurement of radiated emissions inside an ALSE; coupler and oscilloscope shown in inset.

the radiated emissions calculated from the measurements with the directional coupler.

The coupling path or transfer function from the HV line to the test receiver is measured once as the scattering parameter  $S_{21}$  by a VNA and deembedded to the beginning of the HV line (denoted  $S_{21,d}$ ). While the HV system is excited with different signals representing different operation conditions, the obtained wave quantities in the calibration plane  $a_2$  and  $b_2$  are transformed into the deembedding plane as well by

$$a_d = a_2 \cdot e^{-\gamma l}, \quad b_d = b_2 \cdot e^{\gamma l} \quad (14)$$

where  $\gamma = \alpha + j\beta$  is the propagation constant of the HV line and  $l$  is the physical distance between calibration and deembedding plane. Utilizing the deembedded  $S_{21,d}$ , the wave quantity  $b_{EMI}$  at the input of the EMI receiver can be calculated. Care has to be taken to renormalize  $a_d$  and  $b_d$  to the same impedance as  $S_{21,d}$ , usually  $50 \Omega$ . Hence

$$b_{EMI} = \frac{S_{21,d}}{2} \left( \sqrt{\frac{Z_1}{50 \Omega}} (a_d + b_d) - \sqrt{\frac{50 \Omega}{Z_1}} (a_d - b_d) \right) \quad (15)$$

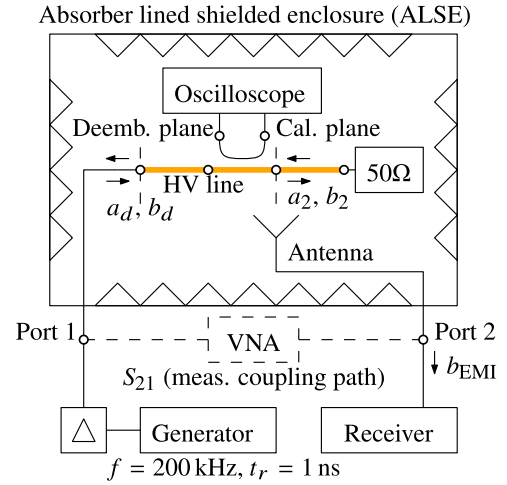


Fig. 17. CISPR 25 related setup for emission measurement.

where  $Z_1$  is the assumed system impedance in the calibration plane. From  $b_{EMI}$  the voltage at input of the EMI receiver can be calculated that would be present if a conventional radiated emission measurement was to be performed under the same operating condition.

The resulting spectra are shown in Fig. 18, where the antenna factor has been utilized to determine the field strength of the electrical field  $E$ . The nondeembedded coupling path  $S_{21}$  is also depicted. Furthermore, the limits for the field strength taken from CISPR 25 [6] are plotted for reference. The results of the presented measurement system and the test receiver show an excellent agreement. The knowledge of the coupling path ( $S_{21}$ ) inside the ALSE is sufficient to accurately predict radiated emissions under different operating conditions if the source quantities were characterized by the presented measurement procedure. The measurements of the wave quantities  $a_2$  and  $b_2$  on the HV line using the oscilloscope do not require an ALSE. Alternatively, the proposed approach can also be advantageously applied to conducted emissions, where the coupling path is then measured between the involved components.

### B. Determination of Load Impedances

Since the presented measurement procedure determines voltage and current in the same calibration plane [see (12)], this data can be exploited to calculate the impedance  $Z_C$  of the load transformed into the calibration plane:

$$Z_C(f) = V_2(f)/I_2(f). \quad (16)$$

If the line impedance and the propagation constant of the HV line are known,  $Z_C$  can be transformed from the calibration plane to the load by applying the transmission line theory [11] to yield the complex impedance  $Z_L$  of the load itself, as shown in Fig. 5. Results from performing this calculations utilizing the measurement setup from Fig. 17 with  $Z_L = 50 \Omega$  are shown in Fig. 19. It can be seen that even for frequencies as low as 10 MHz, the HV line of a length of 1 m cannot be considered electrically short, thus, the impedance  $Z_C$  is not an accurate

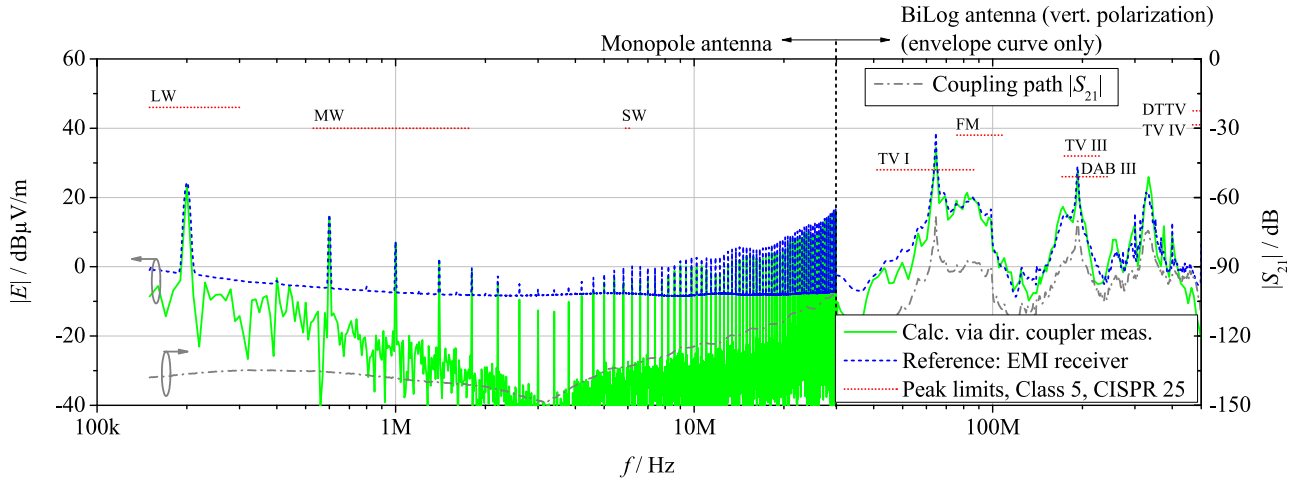


Fig. 18. Radiated emissions: predicted versus reference measurement and the nondeembedded  $S_{21}$  of the coupling path. LW: long wave, MW: medium wave, SW: short wave, FM: frequency modulation, DAB: digital audio broadcasting, TV: television, DTTV: digital terrestrial television.

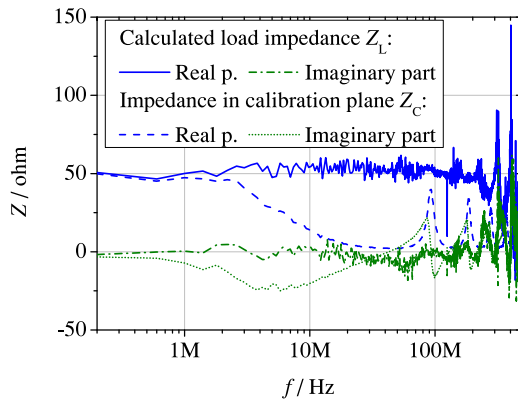


Fig. 19. Measured impedance in the calibration plane and calculated load impedance  $Z_L$  of the 50- $\Omega$  termination.

representation of the actual load impedance. However, transforming  $Z_C$  into  $Z_L$  results in the expected impedance of 50  $\Omega$  up to 300 MHz. Therefore, it is proven that the measurement procedure is also suited to determine load impedances from waveforms that are present during regular operation of HV networks.

## VIII. CONCLUSION

This paper presents a general procedure to quantify RF voltage and current and has been used to precisely determine electromagnetic disturbances in HV power networks in vehicles. A novel calibration procedure is presented that eliminates additional calibration steps such as a separate power calibration, exploits the dynamic range of a VNA and enables reconstruction of time-domain voltage and current waveforms, referencing both to a defined calibration plane. By applying a newly developed automotive-grade directional line coupler, designed for a frequency range from 150 kHz to 1 GHz, undistorted broadband measurements of voltages, currents, and load impedances in a vehicle under real operating conditions become possible. There

is no need anymore to insert non-RF-optimized measurement adapters that could cause misleading signal distortion. By this, accurate values of the EMI relevant noise voltages and currents are measured regardless of the source of the disturbances (battery, power electronics, motor, etc.). This allows the prediction of radiated emissions in a CISPR 25 related setup. The presented measurement system consisting of the HV coupler and the calibration algorithm may also be a helpful means to support ongoing standardization such as ISO 7637-4, the development of EMC filters or the simulation of HV power networks.

## REFERENCES

- [1] S. Guttowski, S. Weber, E. Hoene, W. John, and H. Reichl, "EMC issues in cars with electric drives," in *Proc. IEEE Int. Symp. Electromagn. Compat.*, vol. 2, Aug., 2003, pp. 777–782.
- [2] M. Reuter, S. Tenbohlen, and W. Kohler, "The influence of network impedance on conducted disturbances within the high-voltage traction harness of electric vehicles," *IEEE Trans. Electromagn. Compat.*, vol. 56, no. 1, pp. 35–43, Feb. 2014.
- [3] M. Reuter, S. Tenbohlen, and W. Kohler, "Influence of a traction battery's input impedance on conducted emissions of an automotive HV inverter," in *Proc. Int. Symp. Electromagn. Compat.*, Sep. 2013, pp. 229–234.
- [4] M. Reuter, T. Friedl, S. Tenbohlen, and W. Kohler, "Emulation of conducted emissions of an automotive inverter for filter development in HV networks," in *Proc. IEEE Int. Symp. Electromagn. Compat.*, Aug. 2013, pp. 236–241.
- [5] S. Niedzwiedz and S. Frei, "Transient emission analysis of EV- and HEV-powertrains using simulation," in *Proc. 2013 Int. Symp. Electromagn. Compat.*, Sep. 2013, pp. 247–252.
- [6] *Radio Disturbance Characteristics for the Protection of Receivers Used on Board Vehicles, Boats, and on Devices – Limits and Methods of Measurement*, CISPR Std. 25 Ed. 3, 2008.
- [7] J. Hohloch, S. Tenbohlen, W. Kohler, M. Aidam, and T. Krauss, "Measurement of conducted interferences in automotive high-voltage power networks," in *Proc. EMC Eur. 2011*, Sep. 2011, pp. 224–227.
- [8] D. Ward and J. L. T. Exon, "Using Rogowski coils for transient current measurements," *Eng. Sci. Edu. J.*, vol. 2, pp. 105–113, 1993.
- [9] J. Nelson and M. Aidam, "HEV system EMC investigation during transient operations," in *Proc. 18th Int. Zurich Symp. Electromagn. Compat.*, 2007, pp. 205–208.
- [10] J. Nelson, W. Goodwin, M. Steffka, W. Ivan, and M. Kopp, "High voltage automotive EMC component measurements using an artificial network," in *Proc. 18th Int. Zurich Symp. Electromagn. Compat.*, 2007, pp. 195–200.
- [11] D. Pozar, *Microwave Engineering*, 2nd ed. New York, NY, USA: Wiley, 1998.

- [12] M. Hiebel, *Fundamentals of Vector Network Analysis*. Munich, Germany: Rohde & Schwarz, 2007.
- [13] A. Rumiantsev and N. Ridler, "VNA calibration," *IEEE Microw. Mag.*, vol. 9, no. 3, pp. 86–99, Jun. 2008.
- [14] D. Vye, "Fundamentally changing nonlinear microwave design," *Microw. J.*, vol. 53, no. 3, pp. 22–44, 2010.
- [15] J. Verspecht, "Calibration of a measurement system for high frequency nonlinear devices," Ph.D. dissertation, Vrije Universiteit Brussel, Brussels, Belgium, 1995.
- [16] A. Ferrero and U. Pisani, "An improved calibration technique for on-wafer large-signal transistor characterization," *IEEE Trans. Instrum. Meas.*, vol. 42, no. 2, pp. 360–364, Apr. 1993.
- [17] J. Benedikt, R. Gaddi, P. Tasker, and M. Goss, "High-power time-domain measurement system with active harmonic load-pull for high-efficiency base-station amplifier design," *IEEE Trans. Microw. Theory Tech.*, vol. 48, no. 12, pp. 2617–2624, Dec. 2000.
- [18] M. Gamal el Din, *Load Modulation for Efficiency Enhancement of Switched-Mode Power Amplifiers*. Hannover, Germany: Druck-Team, 2013.
- [19] K. El-Akhdar, S. Ahmed, T. Reveyrand, G. Neveux, D. Barataud, and J. Nebus, "High resolution wideband calibration procedure for RF time-domain measurement of non-linear devices," in *Proc. 81st ARFTG Microw. Meas. Conf.*, Jun. 2013, pp. 1–4.
- [20] K. El-Akhdar, G. Neveux, D. Barataud, and J. Nebus, "Calibrated oscilloscopic system for RF time-domain characterization of non-linear devices," in *Proc. 13th Mediterranean Microw. Symp.*, Sep. 2013, pp. 1–4.
- [21] S. A. Dyer, Ed., *Wiley Survey of Instrumentation and Measurement*. New York, NY, USA: Wiley, 2001, pp. 483–486.
- [22] J. S. Lim and A. V. Oppenheim, Eds., *Advanced Topics in Signal Processing*. Englewood Cliffs, NJ, USA: Prentice Hall, 1988.
- [23] A. V. Oppenheim and R. W. Schaffer, *Digital Signal Processing*. Englewood Cliffs, NJ, USA: Prentice Hall, 1975.
- [24] T. Zelder, B. Geck, M. Wollitzer, I. Rolfes, and H. Eul, "Contactless vector network analysis with printed loop couplers," *IEEE Trans. Microw. Theory Tech.*, vol. 56, no. 11, pp. 2628–2634, Nov. 2008.
- [25] T. Zelder and B. Geck, "Contactless scattering parameter measurements," *IEEE Microw. Wireless Compon. Lett.*, vol. 21, no. 9, pp. 504–506, Sep. 2011.
- [26] Rosenberger Hochfrequenztechnik GmbH & Co. KG. (2012). Rosenberger HVR measurement coupler. Data sheet. [Online]. Available: <http://www.rosenberger.de>
- [27] C. Zietz, G. Armbrrecht, T. Schmid, B. Geck, and M. Wollitzer, "Messverfahren zur Bestimmung der EMV-relevanten Störanteile in Hochvolt-Bordnetzen von Kraftfahrzeugen," presented at the Internationale Fachmesse und Kongress für Elektromagnetische Verträglichkeit, Düsseldorf, Germany, 2014.
- [28] C. Zietz, G. Armbrrecht, T. Schmid, B. Geck, M. Wollitzer, T. Zorn, A. Ludwig, and M. Aidam, "Ein kalibrierbares Messsystem zur transienten Charakterisierung von Hochvolt-Bordnetzen in Fahrzeugen," presented at the 6. GMM-Fachtagung Elektromagnetische Verträglichkeit in der Kfz-Technik, Stuttgart, Germany, 2013.
- [29] A. Radchenko, V. Khilkevich, N. Bondarenko, D. Pommerenke, M. Gonsler, J. Hansen, and C. Keller, "Transfer function method for predicting the emissions in a CISPR-25 test-setup," *IEEE Trans. Electromagn. Compat.*, vol. 56, no. 4, pp. 894–902, Aug. 2014.



**Gunnar Armbrrecht** (S'05–M'12) was born in Seesen, Germany, in 1978. He received the Dipl.-Ing. and Dr.-Ing. degrees in electrical engineering from the Leibniz Universität Hannover, Hannover, Germany, in 2005 and 2010, respectively.

From 2005 to 2010, he was a Research Assistant with the Institute of Radiofrequency and Microwave Engineering, Leibniz Universität Hannover. Since 2011, he has been a Research Engineer with the Rosenberger Hochfrequenztechnik GmbH & Co. KG, Fridolfing, Germany. Today, he is responsible

for the "Advanced Research" activities and acts as the Deputy Head of the research and development division at Rosenberger. His current research interests include automotive applications and include topics such as the signal integrity of high-speed data transmission as well as EMC related topics of high-voltage power networks in electric and hybrid vehicles.

Dr. Armbrrecht received the 2010 Richard Schulz Transactions Prize Paper Award of the IEEE Electromagnetic Compatibility (EMC) Society for the best IEEE/EMC journal contribution in 2009. In 2012, he also received the award for his doctoral (Ph.D.) thesis from the "Stiftung Industrieforschung," a German foundation that supports young researchers who scientifically devote themselves to crucial research questions concerning medium-sized industrial enterprises.



**Thomas Schmid** (M'09) received the Dipl.-Ing. (FH) degree in electrical engineering with emphasis on communication technology from the Munich University of applied sciences, Munich, Germany, in 1996.

Since his diploma thesis on the development of a test setup for the detection of intermodulation distortion on passive devices, he is with Rosenberger Hochfrequenztechnik, Fridolfing, Germany, where he is currently working at the R&D Department as the Head of the EMC and Signal Integrity Laboratory. He is also responsible for the EMC related standard-

ization activities of the company within the IEC TC46. Mr. Schmid received the IEC 1906 Award in 2012 for his contributions to the standardization of different screening effectiveness test methods.



**Michael Wollitzer** (M'98) received the Dipl.-Ing. degree in 1993 and the Dr.-Ing. degree in 1998, both in electrical engineering from Technical University Munich, Munich, Germany.

He was with former Daimler-Benz Research Center in Ulm from 1993 to 1998. Research topics were generation of millimeter-wave signals and near-range radar sensing for automotive applications. Since 1998, he is with Rosenberger Hochfrequenztechnik, Fridolfing, Germany, developing solutions for on-wafer probing, calibration and copper-bound solutions for coax and differential signal transmission. He holds around 15 patents and is author or coauthor of 30 papers.



**Bernd Geck** (M'10) was born in Oldenburg, Germany, in 1959. He received the diploma in electrical engineering and the Dr.-Ing. degree from the Leibniz Universität Hannover, Hannover, Germany.

From 1987, he worked as a Research Assistant and Senior Engineer at the Institute of Radiofrequency and Microwave Engineering. Since 2010, he has been the Technical Head of the Institute. His current research interests include high-frequency measuring and sensor systems and Radio Frequency Identification (RFID) applications. In 2011, he cofounded Triovacos GmbH, which is involved in RFID and Near Field Communication.



**Christian Zietz** (S'09) was born in Hannover, Germany, in 1983. He received the Diplom-Ingenieur degree in electrical engineering from the Leibniz Universität Hannover, Hannover, Germany, in 2009.

Since then, he has been a Research Assistant at the Institute of Radiofrequency and Microwave Engineering, Leibniz Universität Hannover. His research interests include the application of microwave measurement principles to EMC issues and contactless nonlinear vector network analysis.

Mr. Zietz received the EADS Argus Award and the E.ON Future Award for his Diploma thesis and as member of a research consortium the EEEfCOM Innovation Award for contributions on "Advances in Industrial Radar Level Measurements" in 2009. He also received the Best Paper Award at the EMV 2014 in Düsseldorf, Germany.